

Ion density and current distributions in a propagating current sheet, determined by microwave reflection technique

By W. R. ELLIS† AND R. G. JAHN

Department of the Aerospace and Mechanical Sciences, Princeton University, Princeton, N.J.

(Received 7 July 1968 and in revised form on 17 December 1968)

Electron and ion density distributions and the problem of electron/ion current partitioning are studied in a large radius *Z*-pinch in argon. Radial scans of the electron density and temperature profiles in the propagating sheet are obtained with a multi-purpose microwave interferometer which measures the complex reflexion coefficient from the plasma. At 70 GHz the probe resolves densities up to 10^{17} cm^{-3} over dimensions of $\sim 4 \text{ mm}$. Profiles of the electric and magnetic field components are obtained using standard probe techniques, and these data are used to calculate ion and electron current components in the sheet.

Within the approximations of MHD theory, calculations show that the overall axial current pattern is built up of four interior zones alternately dominated by electron or ion current. This structure is observed to be closely correlated with variations of the Hall parameter, ω_b/ν_c , about the value of unity through the sheet, which suggests that this parameter might be used as a guide to the relative importance of ion conduction in pinch discharge current sheets.

1. Introduction

Travelling current sheets of the type encountered in pulsed plasma accelerators or magnetic compression experiments have been shown to differ from more conventional discharges in the relative importance of ion conduction to the overall current density pattern (Lovberg 1963; Lovberg 1966; Johansson 1965; Bodin, Newton & Peacock 1961). Unlike simple low current discharges, where the ion and electron current components may be expected to scale in proportion to the respective scalar mobilities, intense current sheets involve self-induced magnetic fields large enough to drive the electron Hall parameter, $\Omega_e = \text{electron gyro-frequency/electron collision frequency}$, beyond unity, thereby preferentially restricting the electron current to a magnitude comparable to, or even less than, the ion current. The question of current partitioning is also related to other kinetic processes of interest, such as the dynamics of the current sheet, and the ionization and acceleration of the overrun gas. In a more macroscopic view, the relative importance of ion current bears on the dynamical efficiency of the acceleration process, the extent of energy loss and erosion at the electrodes, and the onset of hydromagnetic instabilities (Bodin & Newton 1963).

† Present address: Culham Laboratory, Abingdon, Berks., England.

In this paper we investigate the partitioning of current between electrons and ions in a z-pinch machine. The electromagnetic acceleration processes which sustain the current sheet embody interlocking aspects of compressible gas dynamics, ionized gas physics, electromagnetic field theory, and particle electrodynamics, all of which contribute to great difficulties in formulating an adequate theory of current sheet structure. We will assume a fluid representation here, which allows the currents to be derived from a generalized Ohm's law for the plasma, and the requisite MHD parameters are reviewed in §2. Section 3 deals with the discharge device, and §4 describes the measurements, which consist of obtaining electron density and temperature distributions in the sheet, and profiles of the interior electric and magnetic fields.

The mapping of electron density in a current sheet presents some special problems, e.g. spatial resolution of a few mm in all directions plus sensitivity over a wide range of densities up to 10^{17} cm^{-3} . The microwave techniques developed for the density and temperature measurements are described in §4.

Refinements to the fluid model of the current sheet, based on the experimental data, are examined in §5. Forces acting on the ion fluid are ordered, and electron and ion currents are plotted from the experimental data. The resulting current pattern is found to have a layered structure, which is empirically related to the Hall parameter.

2. Parameters of the problem

In order to obtain serviceable relations between the plasma currents and measurable quantities, one can begin with the MHD charge transport equation for an ionized gas (Sutton & Sherman 1965) (MKS units),

$$\mathbf{j} = \sigma_0 \left[\mathbf{E} + \mathbf{V} \times \mathbf{B} + \frac{\nabla P_e}{n_e e} \right] - \frac{\Omega_e}{|B|} \mathbf{j} \times \mathbf{B} + (1 - \alpha)^2 \frac{\Omega_e \Omega_i}{|B|^2} [(\mathbf{j} \times \mathbf{B}) \times \mathbf{B} - \nabla P_e \times \mathbf{B}] \quad (1)$$

which relates the total current density \mathbf{j} to the electric and magnetic fields \mathbf{E} and \mathbf{B} , the scalar conductivity σ_0 , the fractional degree of ionization α , the electron pressure P_e , the electron density n_e , the electron and ion Hall parameters Ω_e , Ω_i , the proton charge e , and the mass average gas velocity,

$$\mathbf{V} = (m_e \mathbf{V}_e + m_i \mathbf{V}_i + m_n \mathbf{V}_n) / (m_e + m_i + m_n), \quad (2)$$

where the subscripts e , i , n refer to electrons, ions, and neutrals respectively. The first term of (1) represents the effect of electric fields, pressure gradients, and motional EMF in driving the currents, the second term is the Hall effect, and the third term is the so-called 'ion-slip' effect. This last contribution arises in the event of vanishingly few collisions between ions and neutrals, which gives rise to different flow velocities, and hence a net ion current in a co-ordinate system moving with the mass average fluid velocity. We will assume here that any neutrals in the current sheet are tightly collision coupled to the ion stream (see §5), in which case (1) takes the simpler form

$$\mathbf{j} = \sigma_0 \left(\mathbf{E} + \mathbf{V}_i \times \mathbf{B} + \frac{\nabla P_e}{n_e e} \right) - \frac{\Omega_e}{|B|} \mathbf{j} \times \mathbf{B} \quad (3)$$

in which only the ion velocity appears. The components of V_i in the sheet can be calculated from (3) if the net current density, the E and B fields, and the parameters P_e , n_e , Ω_e , and σ_0 can be determined.

The components of E and B can be measured directly by standard probing techniques, and yield, via Maxwell's equations, the net current density j and, in principle, the net charge density $n_i - n_e$. Similarly, the microwave probe to be described yields direct measurement of the two quantities n_e and ν_c , the effective electron collision frequency for momentum transfer. For the ionization levels of interest ($> 0.1\%$), Coulomb collisions dominate over electron-neutral collisions and ν_c can be identified with the Spitzer electron-ion collision frequency (Heald & Wharton 1965; Spitzer 1962)

$$\nu_c = \nu_{ei} = \frac{2.9 \times 10^{-6} Z n_e (\text{cm}^{-3}) \ln \Lambda}{T_e^{\frac{1}{2}} (\text{eV})}, \quad (4)$$

$$\text{where} \quad \Lambda = \frac{1.55 \times 10^{10} T_e^{\frac{1}{2}} (\text{eV})}{Z n_e^{\frac{1}{2}} (\text{cm}^{-3})}. \quad (5)$$

The logarithm is a slowly varying function, ≈ 6 in these experiments, and Ze is the charge on an ion. Having the density and temperature, the electron pressure can be found from the ideal gas law

$$P_e = n_e k T_e, \quad (6)$$

where k is Boltzmann's constant. The pressure gradient can be calculated from profiles of P_e .

The conductivity in (3) can be expressed with various degrees of sophistication (Sutton & Sherman 1965), but we will use the simple Lorentz form,

$$\begin{aligned} \sigma_0 &= \frac{\gamma_E n_e e^2}{g(0) m_e \nu_c} \\ &= \frac{3.3 \times 10^4 \gamma_E T_e^{\frac{1}{2}} (\text{eV})}{Z \ln \Lambda} (\text{ohm} - \text{m})^{-1} \end{aligned} \quad (7)$$

corrected for the low frequency limit, $g(0) = 3\pi/32$, and the slight effect of electron-electron collisions, $0.582 < \gamma_E < 1$ (Heald & Wharton 1965; Spitzer 1962). The Hall parameter is defined in terms of the same collision frequency,

$$\Omega_e = \frac{\omega_b}{\nu_c} = \frac{2.06 \times 10^{17} \gamma_E B (\text{W/m}^2) T_e^{\frac{1}{2}} (\text{eV})}{Z n_e (\text{cm}^{-3}) \ln \Lambda} \quad (8)$$

and satisfies the identity $\sigma_0 B / \Omega_e = n_e e$. Thus all the plasma parameters in (3) reduce to functions of n_e and T_e (or ν_c) and some fundamental constants, and the task becomes one of measuring these and the field distributions through the sheet as functions of r . Solution of (3) for V_i will then yield the ion current

$$j_i = n_i Z e V_i \quad (9)$$

and since the net j is known, the electron current as well.

3. Discharge device

The dimensions and operating parameters of the z -pinch discharge circuit were chosen to provide well-formed current sheets which are intense, stable, accelerating, and reproducible from shot to shot. The discharge vessel, shown in figure 1, is a glass cylinder 20 cm in diameter and 5 cm high, closed by aluminium

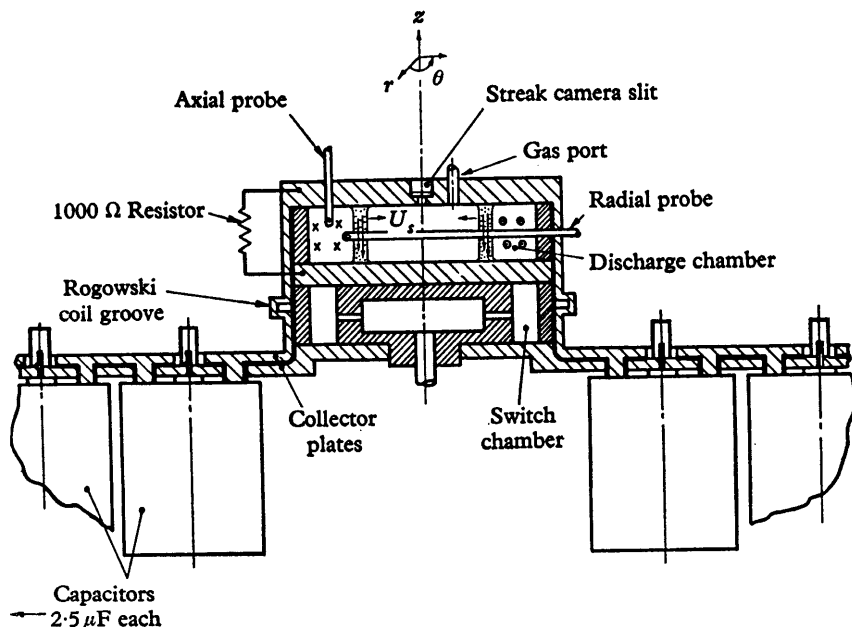


FIGURE 1. Discharge apparatus (schematic).

electrodes 1.9 cm thick. These are fitted with O-ring seals, gas valve, streak camera slot, and a variety of probing ports. Switching is by a low pressure gas triggered discharge, described elsewhere (Jahn *et al.* 1965). For the usual driving currents (200 kA) and argon pressures (0.1 torr), the current sheet is ~ 2.5 cm wide and makes the 10 cm incursion to the axis in $\sim 4 \mu\text{sec}$.

The driving current was programmed to be approximately constant during this time by suitably arranging twenty $2.5 \mu\text{F}$ capacitors along the distributed inductance furnished by two parallel plate transmission lines each 10 ft in length. The resulting bank, which is described elsewhere (Black 1965, 1966), stored 2.5 kJ at 10 kV and yielded a roughly rectangular current pulse of $\sim 200 \text{ kA} \times 5 \mu\text{sec}$ for the experiments.

4. Experimental results

The current waveform is shown in figure 2 as the output of a passively integrated Rogowski coil, together with a streak photograph of the discharge showing its trajectory during the constant current phase. The photograph was taken through the diametral slot in the upper electrode, with a neutral density filter

placed over the centre to reduce the intense luminosity near the axis. The probe measurements to be described were all made as functions of time at $R = 5$ cm, the halfway position of the sheet's radial trajectory to the axis.

Magnetic and electric probe measurements

Magnetic probe loops of conventional design (Huddleston & Leonard 1965), 2 mm in diameter, were introduced into the discharge to measure the time derivative of the magnetic field as the current sheet passed the probes. The usual glass jacket was discarded in favour of a smaller nylon body reinforced with brass, which left the exposed pick-up loop covered with only a thin insulating layer of epoxy (figure 10). The B probes were placed to intercept the current sheet head-on, and aligned to respond to the desired component of \mathbf{B} . The probe response was passively integrated, and calibration was done in position by passing a known current through a central shorting post between the electrodes.

Radial and axial surveys of all three magnetic field components in the sheet revealed a high degree of axial symmetry in the total current distribution, except near the anode where the patterns became generally more complex, diffuse, and sometimes bifurcated (Jahn *et al.* 1968). The investigation was accordingly concentrated between the cathode and centreplane. Figure 3 compares, on the same scale, raw data of B_r , B_θ , and B_z near the cathode, together with their time derivatives. The conduction of essentially axial current is shown by the complete dominance of the azimuthal component B_θ .

The axial current density could be calculated from cross-plots of integrated probe data, using Ampere's law,

$$j_z \simeq \frac{1}{\mu_0 r} \frac{\partial(rB_\theta)}{\partial r},$$

in the usual manner; but in addition to being time consuming and inaccurate, because of the need to differentiate experimental data, this method does not permit visualization of j_z in terms of dB_θ/dt and B_θ , the quantities actually measured by the probe. Nor is a simple velocity transformation appropriate, since B_θ does not actually propagate in the pinching process, although its current source does. The net current enclosed at radius R at time t is

$$I_{\text{enc}}(R, t) = \int_0^R 2\pi r j_z(r, t) dr \quad (10)$$

so that the local magnetic field, $B_\theta = \mu_0 I_{\text{enc}}/2\pi R$, and its time derivative are functions of both the sheet velocity U_s , which convects current past the probe, and dI/dt in the external circuit, assuming I_{enc} varies proportionally. Manipulation of these relations leads to the current density in terms of the total current I and direct probe data,

$$j_z(R, t) = \frac{1}{\mu_0 U_s} \left[\frac{B_\theta(R, t)}{I} \frac{dI}{dt} - \frac{dB_\theta}{dt}(R, t) \right], \quad (11)$$

where μ_0 is the permeability of free space. If both the sheet velocity and circuit current are nearly constant during the sheet transit time over the probe, as they are here (e.g. figure 2), then dB_θ/dt determines the current density profile. j_z is

clearly a peaked function in the sheet (figure 3) and calculations show the region, of negative dB_θ/dt behind the main sheet to be due almost entirely to decreases in I after $4\ \mu\text{sec}$. Hence the sheet is 'well formed', and when measured value of j_z are inserted in (10), most of the circuit current is found to pass through the propagating sheet.

The electric field in the sheet was measured with a floating double probe of the Lovberg-Burkhardt type (Huddleston & Leonard 1965; Lovberg 1964; Burkhardt & Lovberg 1962), having a 2 mm electrode spacing (figure 10). The E probe was inserted as a small coaxial line, ending in a central electrode and a concentric outer ring separated by a truncated cone of epoxy. The coaxial construction eliminated magnetic pick-up, but at the expense of increased sensitivity to transverse electric field gradients, due to the finite dimensions of the ring. The probe output was checked against other configurations to ensure that such errors were small.

Time correlation with B_θ was obtained by positioning a magnetic probe at the same axial and radial co-ordinates as the electric probe, but displaced $\sim \frac{1}{2}$ cm azimuthally to avoid mutual interference. Figure 4 shows typical oscillograms obtained in the centreplane, where the axial current distribution, compared to the cathode, is seen to be somewhat wider and less reproducible at the rear of the sheet. The electric field has two components, shown here to the same scale, which are closely correlated in time (position) with the magnetic field and current density. The streamwise component E_r arises from a slight radial displacement of the centroids of the electron and ion density distributions, and reaches a magnitude of $\sim 9000\ \text{V/m}$; E_r supplies a major mechanism for accelerating over-run ions in the plasma from rest to their streaming velocity. The applied field E_z , which reaches about the same amplitude as E_r in the lab frame of reference, is reduced in the sheet frame by $|U_s B_\theta|$ to a maximum of $\sim 3500\ \text{V/m}$. As B_θ increases through the sheet, the transformed E_z reverses sign and closely follows E_r . (The sheet velocity was measured independently from streak photographs, and electric, magnetic, and microwave probe data, and all gave $U_s \approx 25,000\ \text{m/sec}$ at mid-radius, within a few percent.)

The ion density can be related to the electron density from the E probe data and Gauss's law. Since radial gradients far outweigh axial variations in the sheet, this may be written

$$\frac{\partial E_r}{\partial r} \approx \frac{(n_i - n_e)e}{\epsilon_0}. \quad (12)$$

The maximum $n_i - n_e$ is found to be $< 10^{-7}$ of the measured electron number density in the sheet, so that the assumption $n_i = n_e$ could be made with negligible error.

Microwave probe measurements

The electron density and collision frequency were measured with a multipurpose microwave reflexion bridge which returned information on the complex reflexion coefficient from the plasma. This technique (Takeda & Tsukishima 1965; Funahashi & Takeda 1968; Hermansdorfer 1965) is well suited to current sheet studies, because the large reflexions from a plasma above the 'cut-off' density n_c can be used to avoid the usual line-of-sight integration of data which characterizes

lower density transmission interferometry (Heald & Wharton 1965) thus providing maximum three-dimensional space resolution as well as sensitivity to n_e considerably above the usual upper limit of n_c .

In order to relate plasma reflexions to the electron density and temperature, one may begin with the usual manipulation of Maxwell's equations (Heald & Wharton 1965) to obtain the harmonic wave equation for a uniform, isotropic medium of finite conductivity and net charge neutrality,

$$\nabla^2 \mathbf{E} + (k_0 \mu^*)^2 \mathbf{E} = 0, \quad (13)$$

where $k_0 (= 2\pi/\lambda_0 = \omega/c)$ is the vacuum wave-number, ω is the angular frequency of the impressed electric field \mathbf{E} ,

$$\mu^* = \sqrt{\left(1 - \frac{i\sigma}{\epsilon_0 \omega}\right)} = \mu_r - i\mu_i \quad (14)$$

is the complex refractive index of the medium, σ is the electrical conductivity, and ϵ_0 is the vacuum permittivity. The plane wave solutions of (13) are transverse, in the form

$$\mathbf{E} = \mathbf{E}_0 \exp i(\omega t - k_0 \mu^* z) \quad (15)$$

and the wavelength and attenuation in the medium are thus embodied in the conductivity term. The simplest derivation of σ proceeds by identifying an 'ensemble-average' electron, whose drift velocity defines the current per particle and obeys the heuristic equation of motion

$$m_e \frac{d\mathbf{v}_d}{dt} + m_e \nu_c \mathbf{v}_d = -e\mathbf{E} \quad (16)$$

with \mathbf{E} given by (15). Solution of (16) yields

$$\sigma = \frac{n_e e v_d}{E} = \frac{n_e e^2}{m_e (\nu_c + i\omega)} = \epsilon_0 \left(\frac{\omega_p^2}{\nu_c + i\omega} \right) \quad (17)$$

(compare equation (7)) where we have written σ in terms of the electron plasma frequency, $\omega_p = \sqrt{(n_e e^2 / \epsilon_0 m_e)}$, the natural frequency of oscillations of the free electron component. The resonant, or cut-off density is defined by the inverse relation, $n_c = \epsilon_0 \omega^2 m_e / e^2$.

Combining (14) and (17) yields the real and imaginary parts of μ^* ,

$$\mu_r^2 = \frac{1}{2} \left[1 - \frac{(\omega_p/\omega)^2}{1 + (\nu_c/\omega)^2} \right] + \frac{1}{2} \left\{ \left[1 - \frac{(\omega_p/\omega)^2}{1 + (\nu_c/\omega)^2} \right]^2 + \left[\left(\frac{\nu_c}{\omega} \right)^2 \frac{(\omega_p/\omega)^2}{1 + (\nu_c/\omega)^2} \right]^2 \right\}^{\frac{1}{2}}, \quad (18)$$

$$\mu_i^2 = -\frac{1}{2} \left[1 - \frac{(\omega_p/\omega)^2}{1 + (\nu_c/\omega)^2} \right] + \frac{1}{2} \left\{ \left[1 - \frac{(\omega_p/\omega)^2}{1 + (\nu_c/\omega)^2} \right]^2 + \left[\left(\frac{\nu_c}{\omega} \right)^2 \frac{(\omega_p/\omega)^2}{1 + (\nu_c/\omega)^2} \right]^2 \right\}^{\frac{1}{2}} \quad (19)$$

which specify the wave motion in the plasma in terms of the electron density n_e and collision frequency ν_c .

In practice the wave-train must cross interfaces, such as a dielectric window, to reach the plasma, and the resulting probe response involves a solution of the appropriate boundary-value problem (Jahn 1962). The window can be removed

from the calculation, by making it a half-wave plate (Jahn 1960), for example, and the transmission and reflexion coefficients then follow by requiring continuity of the tangential components of the field vectors at the air-plasma interface. For the present problem we are interested in the reflexion coefficient,

$$R^* = E_R/E_I = |R| \exp(i\phi_R),$$

which takes the form (Jahn 1960)

$$|R| = \frac{[(1 - \mu_r^2 - \mu_i^2)^2 + 4\mu_i^2]^{\frac{1}{2}}}{(1 + \mu_r^2)^2 + \mu_i^2}, \quad (20)$$

$$\phi_R = \tan^{-1} \left(\frac{2\mu_i}{1 - \mu_r^2 - \mu_i^2} \right). \quad (21)$$

These quantities are computed and plotted against n_e/n_c in figures 5 and 6, with ν_c/ω as a parameter. For the anticipated small values of ν_c/ω , the reflected amplitude is most sensitive to n_e below n_c , the reflected phase angle to n_e above n_c . This complementary sensitivity means that interference effects can be produced over a wide range of densities when the reflected signal is combined with a suitable reference signal at the detector.

Let the reference signal have the same magnitude as the signal E_I incident on the plasma. The reflected signal is $E_I |R| \exp(i\phi_R)$, and the amplitude A of the interference signal is $E_I \{1 + |R| \exp(i\phi_R)\}$. Referring to the insert in figures 7 or 8, we may write this (in normalized form) as

$$S = \frac{A}{2E_I} = \sqrt{\left(\frac{1 + |R|^2 \pm 2|R| \cos \phi_R}{4} \right)}. \quad (22)$$

Computed interferometer responses are plotted in figures 7 and 8 for the two possible bridge modes, corresponding to a choice of $(-)$ in (22)—mode *A*, where $S \rightarrow 0$ at $n_e = n_c$ and $S \rightarrow 1$ as $n_e \rightarrow \infty$ —and vice versa for $(+)$, mode *B*. The two modes obviously do not produce symmetric signals, and this property is very useful in studying electron density gradients (see Appendix).

At the operating frequency of 70 GHz ($\lambda_0 = 4.28$ mm), the cut-off density is $n_c = 6.1 \times 10^{13} \text{ cm}^{-3}$, about 10^{-2} of the filling density at 0.1 torr. For ionization levels above $\sim 1\%$ there will thus be large reflexions, and from the figures $|R|$ and ϕ_R (or S) are seen to be sufficient to determine n_e and ν_c simultaneously over at least the range $6 \times 10^{12} < n_e (\text{cm}^{-3}) < 10^{17}$ (small ν_c/ω). Note that a quick estimate of the collision frequency can be made from the height of the S spike at $n_e = n_c$, which is very sensitive to ν_c/ω .

The bridge circuit used to measure $|R|$ and S is shown schematically in figure 9. It was operated inside a portable screen room, and for S measurements the reference arm of the interferometer was adjusted to pass a signal equal in magnitude and phase to the reflexion from a metal block placed over the horn.

Unfortunately, the conventional method for measuring $|R|$ —which relies upon directional couplers and E - H tuners to buck out spurious reflexions (Heald & Wharton 1965)—inherently fails when one is confronted with significant two-way transmission of power in the wave-guide. This is because $|R|$ itself can undergo

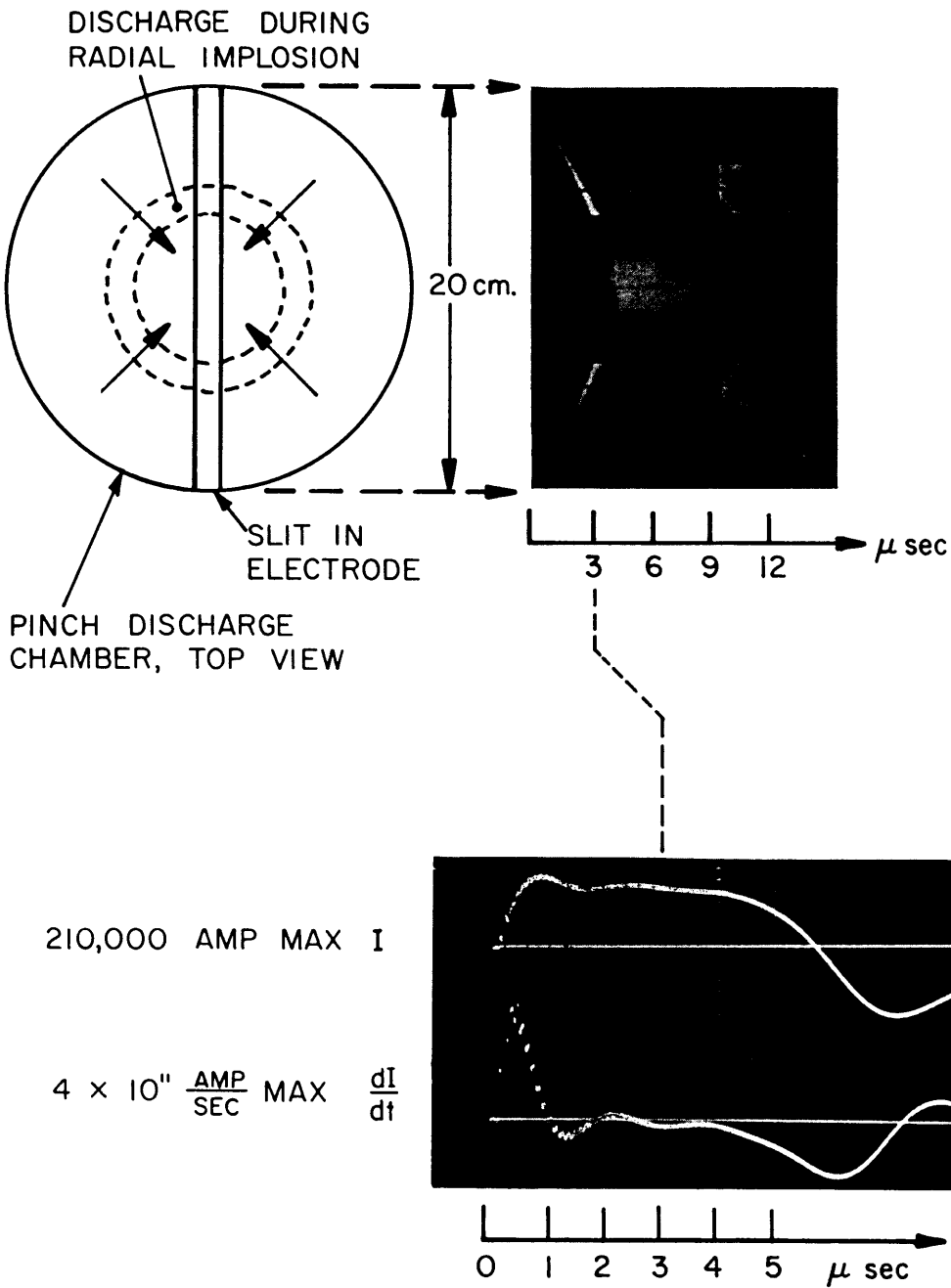


FIGURE 2. Streak photograph of discharge, and current wave-form.

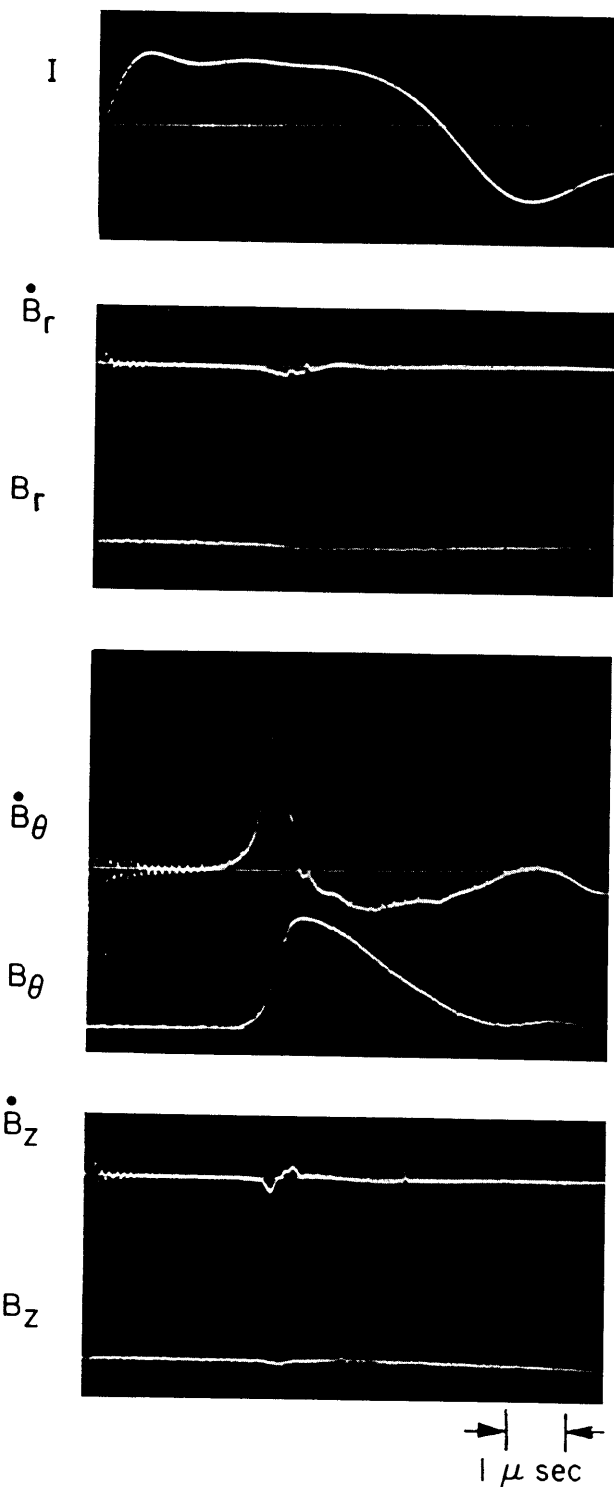


FIGURE 3. *B*-probe data (mid-radius near cathode).

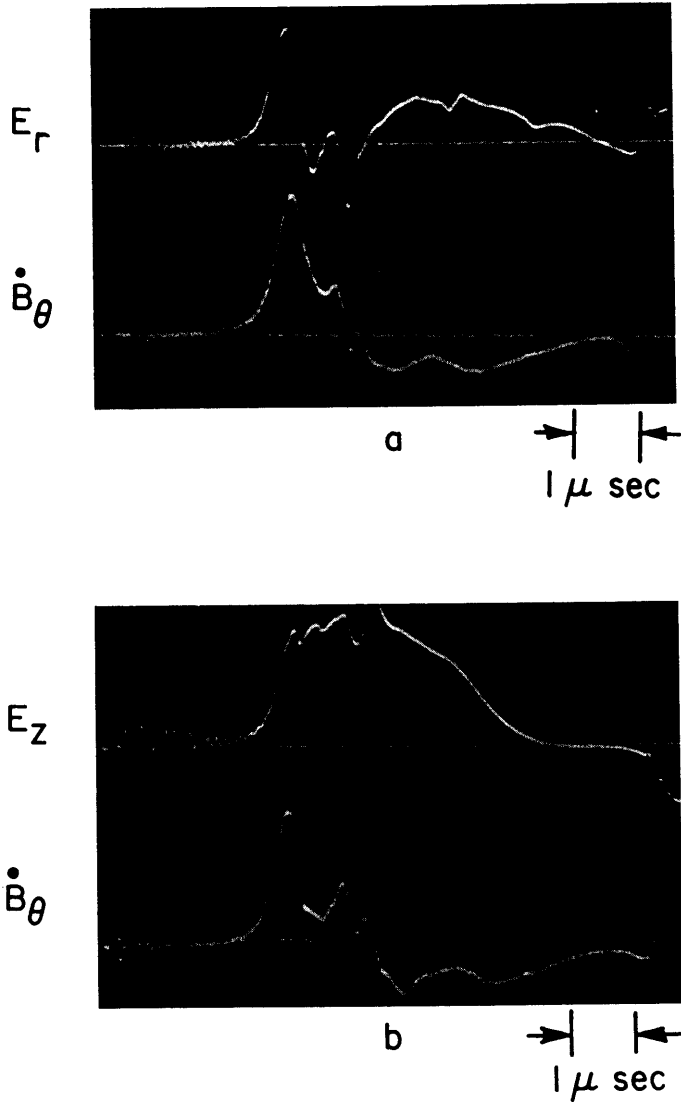


FIGURE 4. *E*-probe data (mid-radius centre plane).

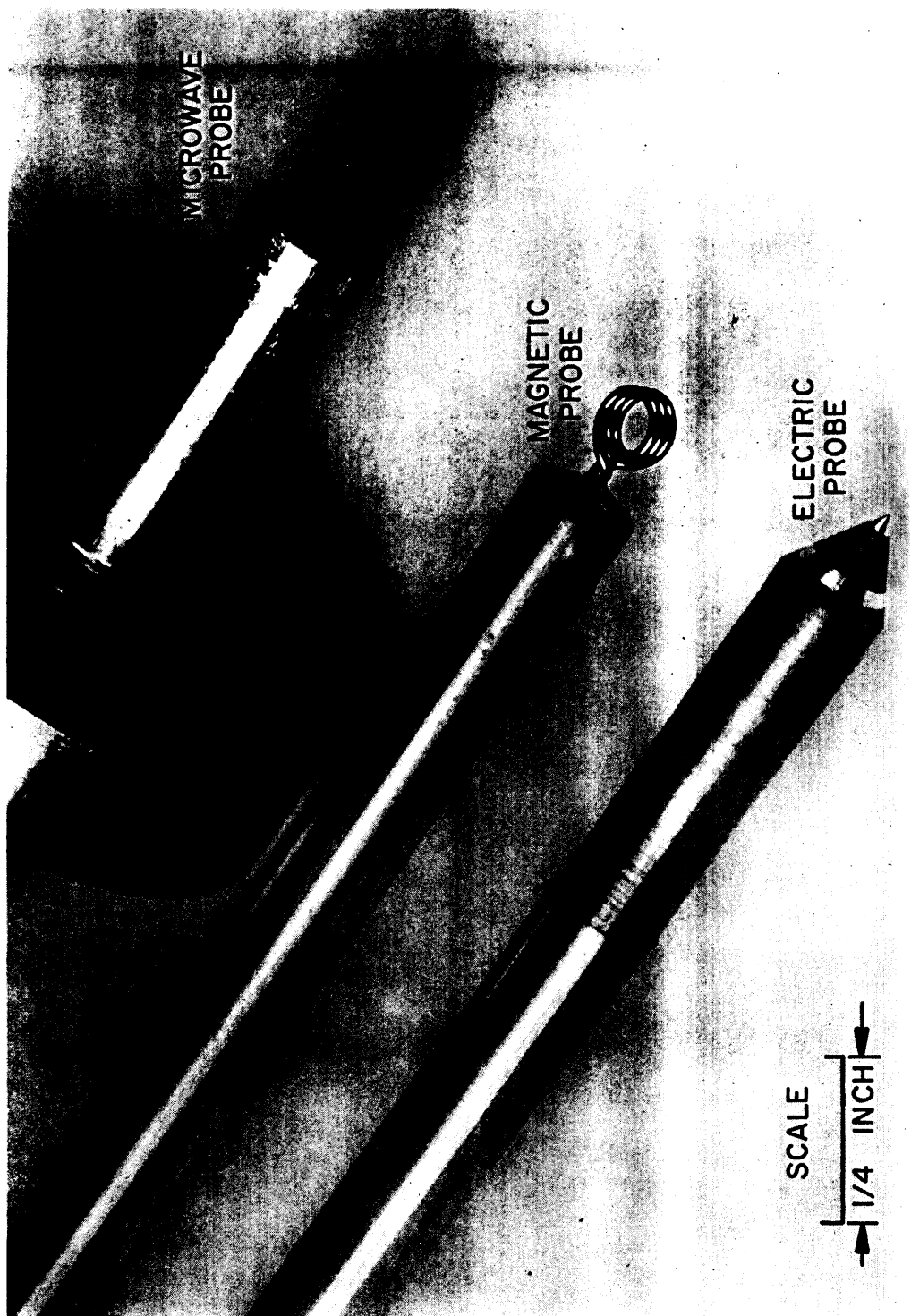


FIGURE 10. Comparison of electric, magnetic and microwave reflection probes.

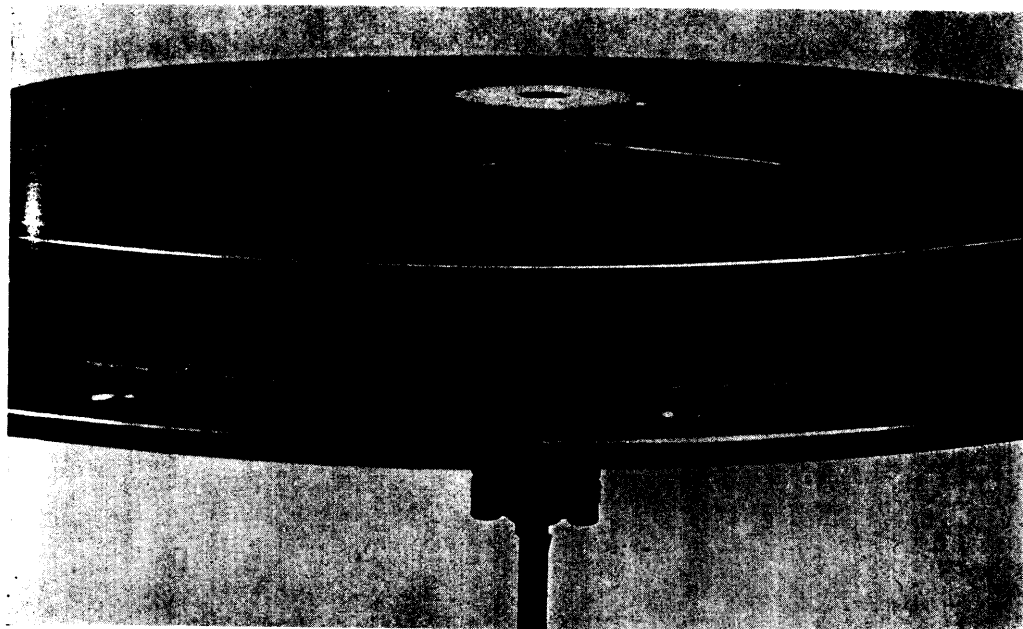
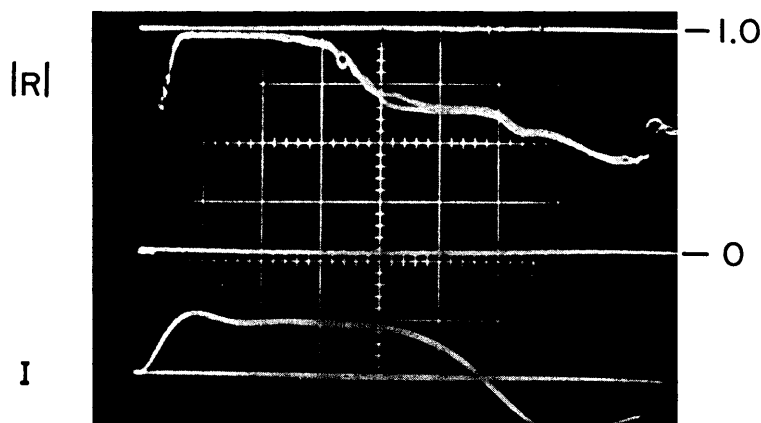
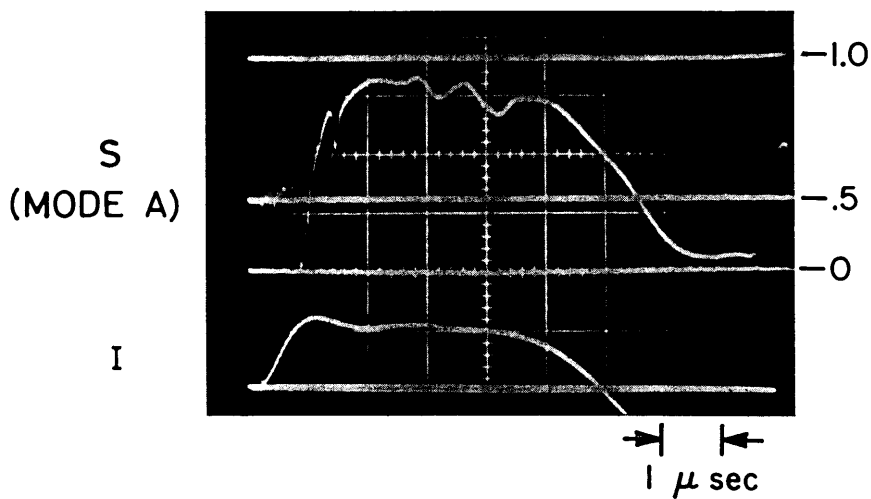


FIGURE 11. Reflexion probe in electrode, with Teflon airfoil.



a) REFLECTED AMPLITUDE



b) REFLECTED PHASE

FIGURE 12. Format of microwave data.

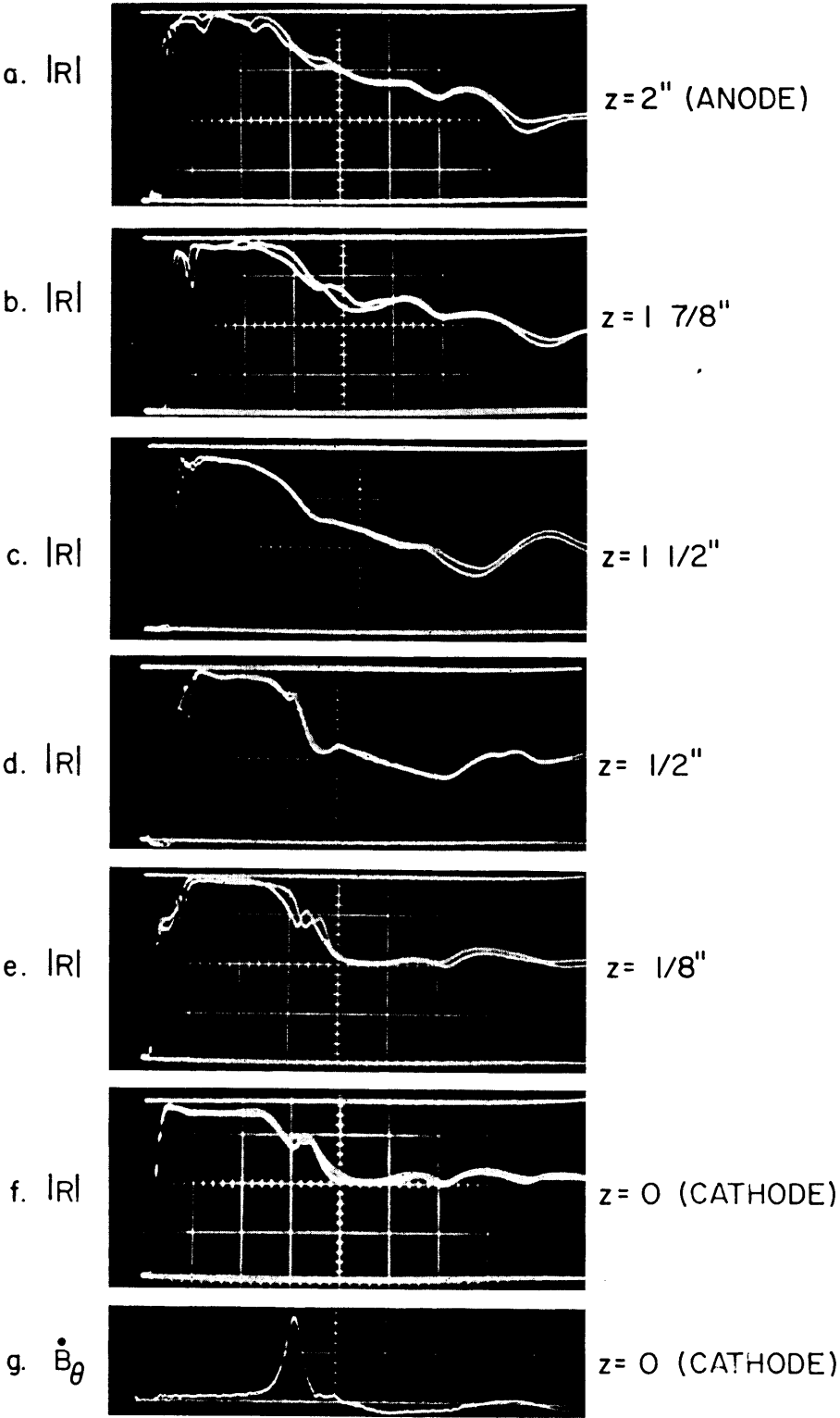


FIGURE 13. Axial $|R|$ survey (mid-radius).

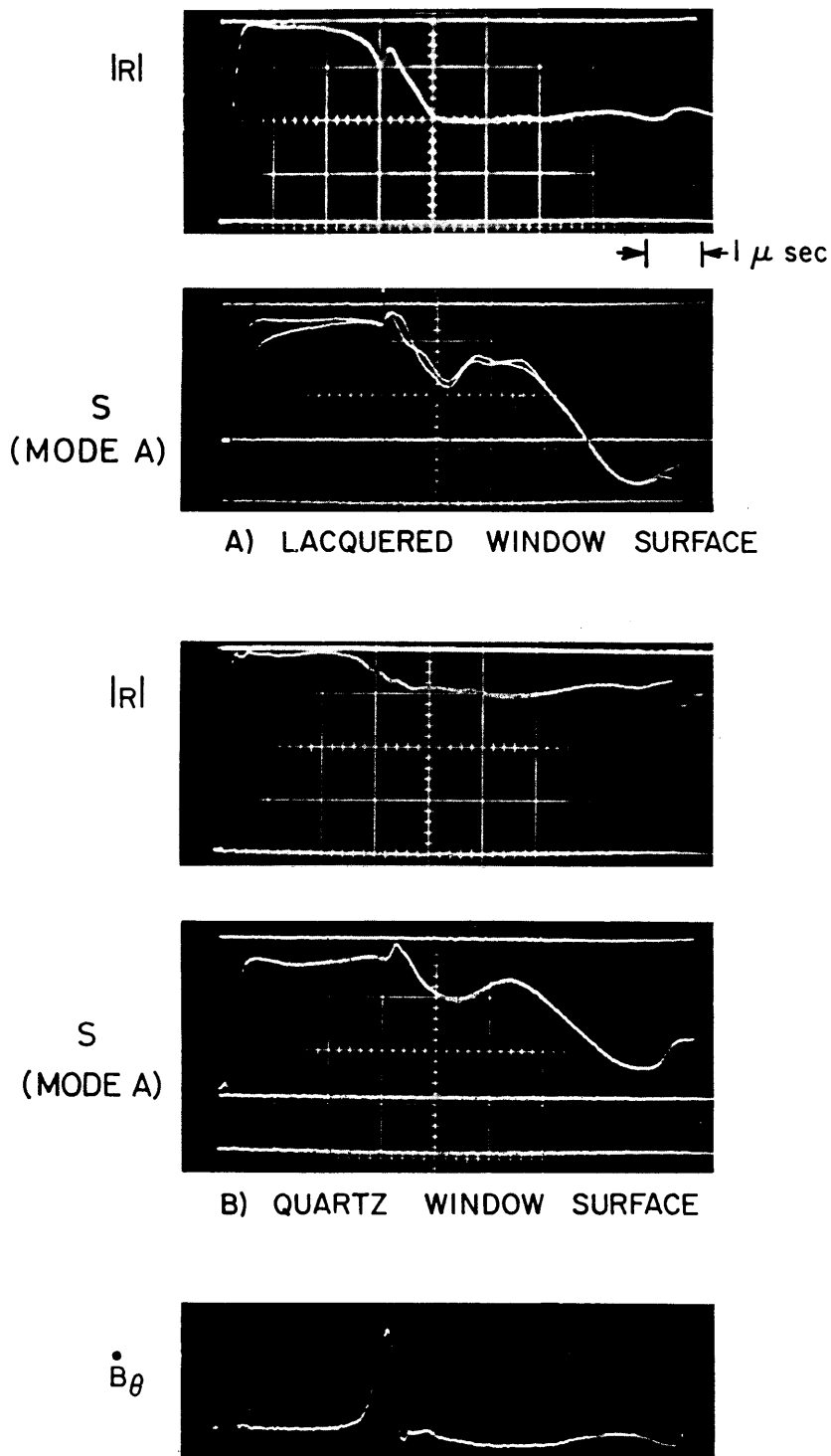


FIGURE 14. Influence of probe on microwave measurables.

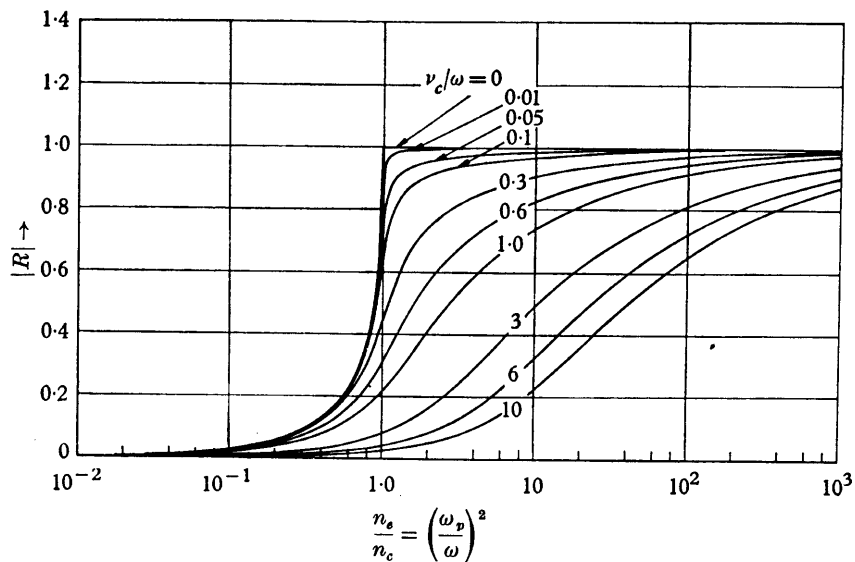


FIGURE 5. Amplitude of reflexions from semi-infinite plasma slab.

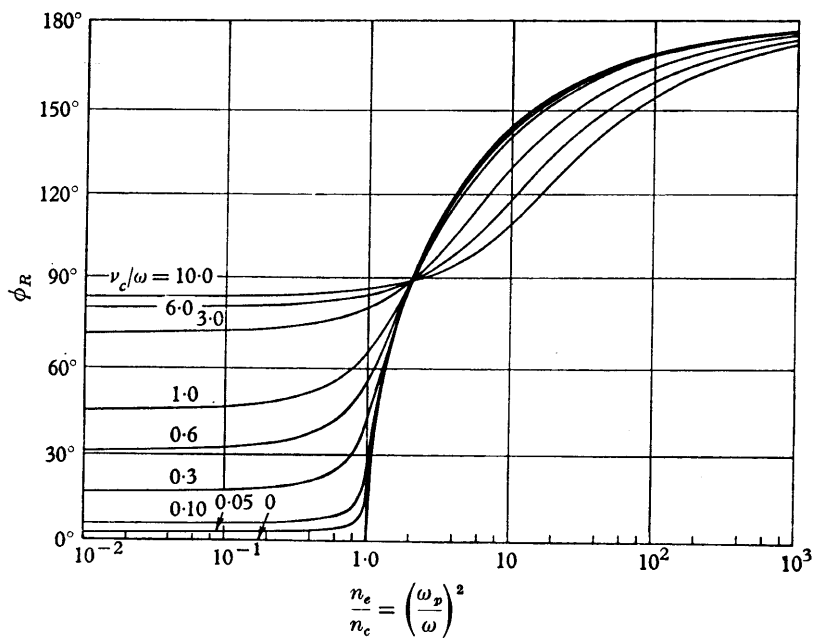


FIGURE 6. Phase angle of reflexions from semi-infinite plasma slab.

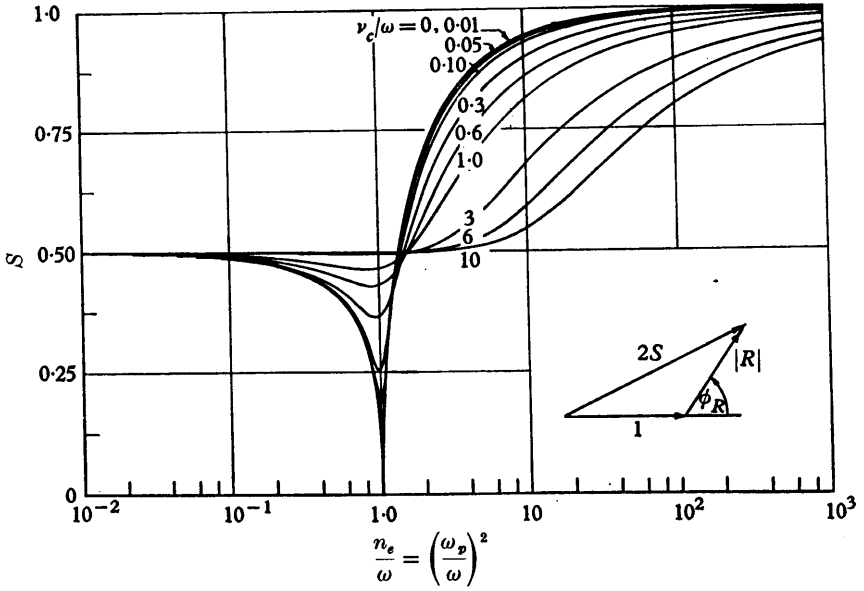


FIGURE 7. Theoretical interferometer response, *A* mode, semi-infinite plasma slab.

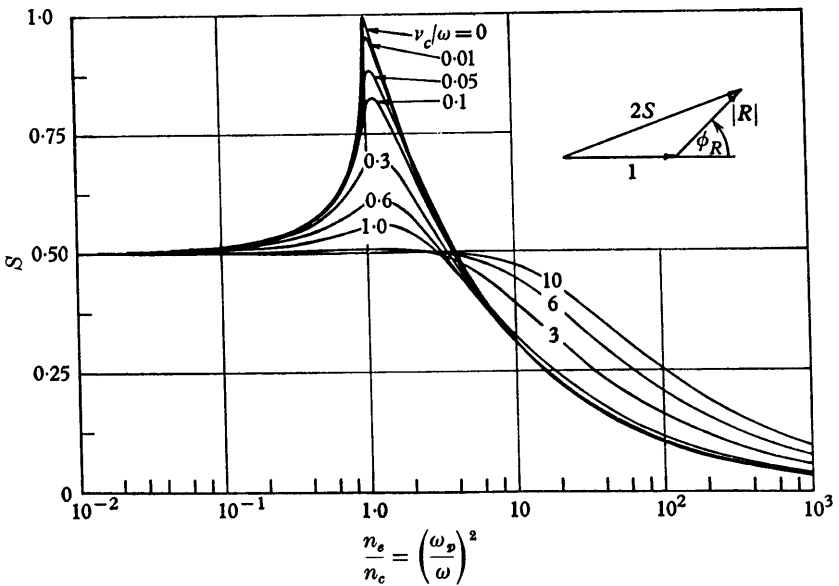


FIGURE 8. Theoretical interferometer response, *B* mode, semi-infinite plasma slab.

substantial internal reflexions, which add vectorially to produce interference effects at the detector. This effect is easily demonstrated by oscillating a metal plunger in the wave-guide, which should theoretically produce a steady reflexion of unit amplitude. To achieve this result in practice, however, it was necessary to return to the bridge circuit of figure 9. By admitting a signal of the correct amplitude and phase from the reference arm, the system could be balanced for large reflexions, and the plunger signal made steady. Subsequent $|R|$ measurements from the plasma showed the desired insensitivity to ϕ_R .

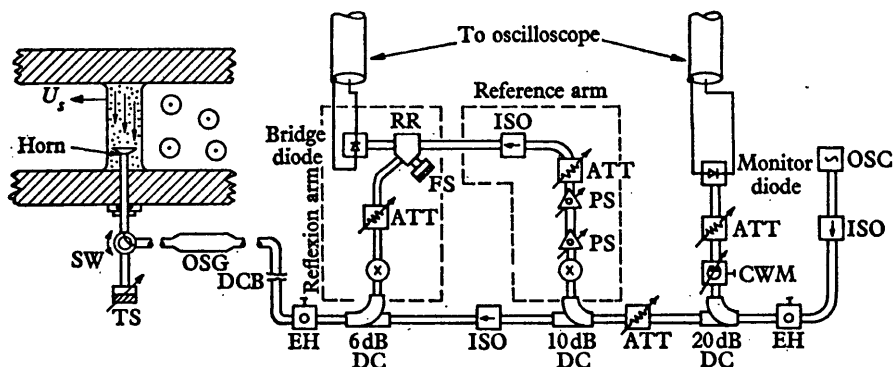


FIGURE 9. Schematic diagram of reflexion bridge. *Notation*: OSC, 70 GHz oscillator, reflex klystron; ISO, ferrite isolator; EH, E and H plane tuner; DC, directional coupler; CWM, cavity wave meter; ATT, variable attenuator; Diode, solid state detector; X, isolation valve for bridge balancing; PS, variable phase shifter; RR, rat race junction; FS, fixed short; DCB, direct current break in wave-guide; OSG, oversize guide; SW, 3-port switch; TS, tunable short for reference reflexions.

All bridge components were standard with the exception of the reflexion horn, shown with representative E and B probes in figure 10. During the experiments the plasma in the current sheet behaved as a nearly perfect reflector to the microwaves, the reflexion coefficient approaching within a few percent of unity. In this condition a wave-train incident on the plasma is reflected with negligible energy leakage, and the plasma interface gives the same reflexion coefficient as if the plasma were inside the wave-guide. The net energy flow is one-dimensional, which leads to results identical with the plane wave analysis above (equations (20) and (21)) (Slater 1959). Since there is no need to launch plane waves, a flared horn is unnecessary, and the horn dimensions need be no larger than the fundamental mode wave-guide, providing a transverse spatial resolution of $\sim \lambda$. The penetration of the wave into the high density plasma is small. For $n_e = 10^{15} \text{ cm}^{-3}$, (19) shows this distance to be less than 1 mm. The influence of B_0 on the skin depth (and also on R^* , see Appendix) is negligible in these experiments.

The horn design† evolved from extensive tests and incorporated a smooth rectangular to circular transition with a quartz window (an exact one-wave plate) mounted flush in the circular aperture. With a matching iris the voltage

† The design and construction of the horn was performed by TRG Inc., Boston, under the supervision of the authors.

standing wave ratio (VSWR) is less than 1.05 : 1 at 70 GHz, giving a residual $|R|$ from the window of less than 2 %. The horn was positioned radially and axially through probing ports in the electrodes, and a Teflon air foil was used to minimize gasdynamic effects at interior positions (figure 11).

Interpretation of microwave data

The format of the data can best be explained with representative $|R|$ and S oscillograms, as shown in figure 12, where two $|R|$ traces are overlaid to show shot-to-shot reproducibility and signal-to-noise ratio. Since the interferometer produces only a fractional fringe ($\Delta\phi_R \leq 180^\circ$), the oscillograms must be calibrated, which requires two reference lines for $|R|$ (0, 1) and three for S (0, $\frac{1}{2}$, 1). The top lines correspond to reflexion from the metal plunger, the bottom lines to zero signal. Placing the $S = \frac{1}{2}$ line (reference arm only) gives the power law response of the diode detector, which lies between linear and square law in the example shown, and makes the probe essentially self-calibrating for every shot.

Reference to figure 12 and the theoretical curves of figures 5 and 7 shows that at early times in the discharge n_e increases monotonically at the horn position. $|R|$ rises rapidly from zero to a cut-off value of ~ 1 as the current increases. At the same time S dips from 0.5 to 0, pinpointing $n_e = n_c$ (at $\sim \frac{1}{2} \mu\text{sec}$), and rises from this null toward unity as n_e goes above n_c . The sharp null shows that $\nu_c/\omega \ll 1$ as expected, a fact which is also inferred from the large value of $|R|$. The current sheet, as detected by B -probes, arrives at the probe position at $\sim 3 \mu\text{sec}$, by which time the electron density is quite high, corresponding to $\sim 10\%$ ionization of the gas ahead of the sheet.

The passage of the current sheet causes further increases in n_e , as shown by the shallow twin peaks in S . These correspond to a bifurcated current distribution near the anode, where these particular data were taken, and as $S \rightarrow 1$ only as $n_e \rightarrow \infty$, the density increases associated with the presence of the sheet are quite large. Quantitative estimates of n_e and T_e require simultaneous data reduction of $|R|$ and S , since damping becomes severe on both traces as the current sheet passes the probe.

The existence of a large electron density for a considerable distance ahead of the propagating sheet is a noteworthy feature, for it indicates an effective means of self-preionization. Possible candidates for this effect could be gas currents, electron diffusion ahead of the sheet, or a front-running precursor shock wave. However, a search with magnetic, electric, and pressure transducer probes appropriate to disclose the presence of these detects none of them (Ellis 1967; York 1968), and it seems more likely that the early high densities are due to photo-ionization of the enclosed gas by radiation from the encircling sheet. This raises the possibility of an interesting 'boot-strap' or feedback process, since a self-preionizing discharge can partially control its own current mechanisms, at least in the leading edge of the sheet, by virtue of advancing into a prepared high density plasma whose transport properties are Coulomb dominated everywhere.

As the sheet passes the probe a pronounced damping is apparent in $|R|$, and to a lesser extent in S , which we interpret as due to a rising collision frequency. Other possibilities were first considered, and in the Appendix it is shown that

changes in the plasma refractive index from B_θ cannot be responsible here, nor can free density gradients near the horn window. Experiments to simulate the plasma showed that the interface could not pull away from the horn window far enough to cause significant signal loss without simultaneously phase shifting the interferometer through a complete additional fringe.

The onset of collisional damping has the axial dependence shown in figure 13 (\dot{B}_θ locates the current). The doubly overlaid traces show the reproducibility of the small variation between adjacent positions. The damping in $|R|$ is about the

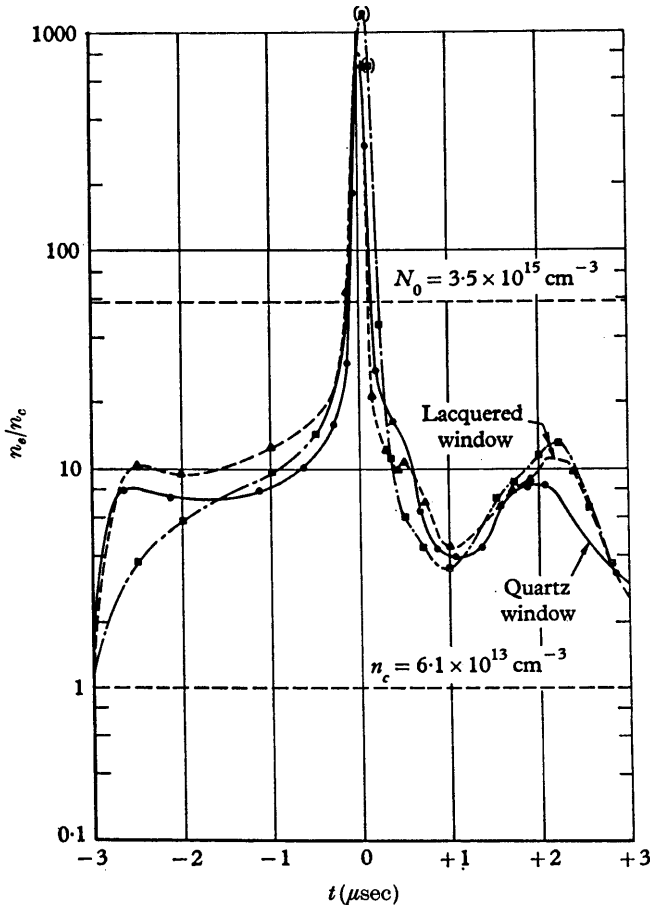


FIGURE 15. Experimental electron density profiles (mid-radius near cathode).

same in each case, $\sim 50\%$, but the Δt (or Δr) over which the change occurs is narrowest at the cathode and widest at the anode, and corresponds to the width of the current sheet at those positions from B probe data.

A straightforward interpretation of such damping decrements is complicated by the fact that they are not entirely due to n_e and T_e variations in the sheet. There is an important contribution from contamination by the probe, as shown in figure 14. Here two $|R|$ and S data sets are compared which are identical except for the horn window used: set A is made with quartz, set B with a thin

clear coat of hard lacquer sprayed over the quartz to reduce erosion (figures 12 and 13 were made this way). There is clearly less damping of the traces for the harder quartz surface, implying that ν_c can be identified with ν_{et} only after this contamination effect has been extrapolated back to zero. This task is greatly simplified by the fact that impurities vapourized from the window by the current sheet do not ionize significantly on the time scale of the experiment, i.e. the measured n_e profiles are independent of the choice of window surface.

Figure 15 shows the experimental $n_e(t)$ profiles obtained from the data of figure 14. Reference lines are shown for the critical and filling densities, and the time origin is taken as the centre of the current sheet. The data scatter here represents the maximum observed, due to the extreme variation in the window material. Ahead of the sheet the ionization reaches 10–15 %, due to the precursor

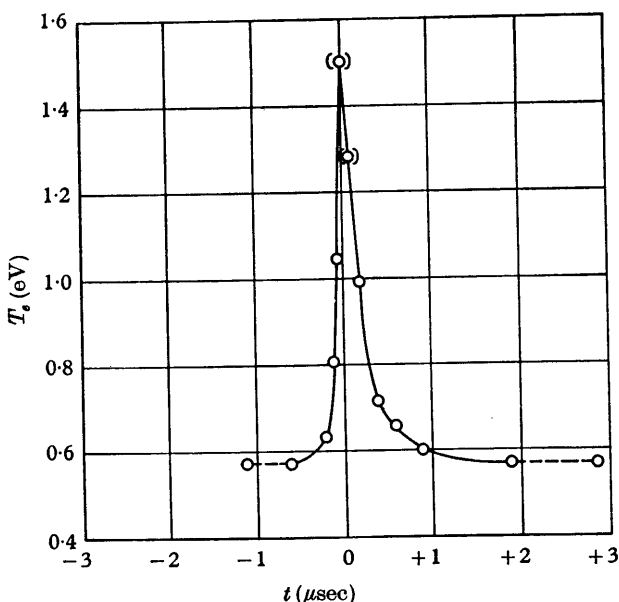


FIGURE 16. Typical electron temperature profile (mid-radius near cathode).

effect already mentioned. In the sheet itself the density exceeds $3 \times 10^{16} \text{ cm}^{-3}$, an order of magnitude above the filling density, indicating a large compression and possibly multiple ionization. In general $n_e(t)$ bears a close resemblance to $j_z(t)$, even duplicating the trailing bump, about 1 % of the big peak, seen by the *B*-probes. It will be shown below, however, that this resemblance does not automatically imply simple electron currents everywhere in the sheet.

The corresponding $T_e(t)$ profiles can be calculated directly from the ν_c/ω data and $n_e(t)$, using (4), once the contamination contribution to ν_c is subtracted out. This can be done graphically in a straightforward way (Ellis 1967), and here we simply present the results.

Figure 16 gives the $T_e(t)$ profile constructed from the data of figure 14. T_e is seen to peak in the sheet at a maximum value of $\sim 1.5 \text{ eV}$, although this value should more strictly be regarded as a lower bound, due to the inherent inaccuracy of the

graphical method. An upper bound of a few eV has been estimated from spectroscopic data and energy balance calculations (Burton & Jahn 1968). However, since T_e changes by only a factor of three while n_e changes by two orders of magnitude, the collision frequency and Hall parameters in the sheet are controlled by n_e . The need for precision is thus somewhat less critical for T_e and the profile of figure 16 was used in all subsequent calculations.

Measured profiles of $n_e(t)$ and $\nu_c(t)$ undergo some broadening and flattening as the probe is moved axially from cathode to anode, similar to the total current profiles, but between cathode and centre plane they do not differ qualitatively from those discussed above.

5. Discussion of models

Having established that $\mathbf{B} = \hat{\theta}B_\theta$, $\mathbf{E} = \hat{r}E_r + \hat{z}E_z$, we can expand (3) in component form and solve the resulting equations simultaneously for the radial and axial total current densities to obtain

$$j_r = \frac{\sigma_0}{1 + \Omega_e^2} \left[\left(E_r + \frac{1}{n_e e} \frac{\partial P_e}{\partial r} - V_{zi} B_\theta \right) + \Omega_e (E_z + V_{ri} B_\theta) \right], \quad (23)$$

$$j_z = \frac{\sigma_0}{1 + \Omega_e^2} \left[(E_z + V_{ri} B_\theta) - \Omega_e \left(E_r + \frac{1}{n_e e} \frac{\partial P_e}{\partial r} - V_{zi} B_\theta \right) \right], \quad (24)$$

The radial pressure gradient has been retained, and it should be noted that it can drive both radial and axial currents, i.e. scalar and Hall modes, just as can the radial and axial electric fields. (Since P_e , like the temperature and density, is peaked in the sheet, $\partial P_e / \partial r$ has opposite signs on either side of the maximum; its greatest contribution to j_z is $\sim 30\%$ in the front half of the sheet.)

The simplest way of solving these equations is to neglect the smaller radial current component and set $j_r = 0$, leaving two equations in the two unknown ion velocities V_{ri} and V_{zi} . This turns out to be a severe assumption, however, for it suppresses any radial separation of electron-ion pairs entering the sheet or created within it, and incorrectly specifies the ion velocity, as we shall see. Furthermore, if we wish to avoid using Ampere's law, $j_r \approx (1/\mu_0) (\partial B_\theta / \partial z)$, which requires differentiating experimental data, then the remaining alternative is to estimate V_{ri} by some means, and solve (23) and (24) for V_{zi} and the radial current density. This is the approach used here.

Consider a co-ordinate system moving with the sheet. We can envisage the flow entering the sheet at velocity U_s , and commencing deceleration and deflexion in the crossed electric and magnetic fields. The entering plasma is $\sim 10\%$ ionized as we have seen, and this fraction increases rapidly as we move further into the sheet. The ion population initially begins a simple deceleration in the opposing E_r field, and simultaneously gains an axial component of velocity V_{zi} along E_z . The ion gyro-radius, $r_i = m_i V_i / e B_\theta$, is several meters in the front part of the sheet where V_i is large and B_θ is still small, which means that the average ion would be only slightly deflected by the magnetic field even if it moved on a collisionless trajectory and was unhindered in its turning motion. The remaining mass resides

in the rapidly diminishing population of neutrals, which would maintain their incoming velocity in the absence of collisions. However, they are tightly collision-coupled to the decelerating ion stream because of the nearly equal masses, so that electromagnetic forces acting on the ions are transmitted via gasdynamic forces directly to the neutrals. As the ions decelerate they move into an ever larger magnetic field, and the two effects combine to reduce the ion gyro-radius at the rear of the sheet to less than 1 cm. Magnetic influences on the ion motion are thus potentially important only toward the rear of the sheet, whereas the much lighter electrons, whose gyro-radius is a fraction of a mm at all measurable values of B_θ , are potentially susceptible to Hall deflexion everywhere in the sheet.

If we take the motion of a typical ion as representative of the mean fluid motion, the ion stream will decelerate less than predicted by E_r alone, since it must also help brake the neutral stream; but on the other hand the ion stream is being increasingly turned by B_θ as it decelerates, and consequently loses more forward velocity than it would in E_r alone. Thus the two effects are in opposite directions, and for a first approximation to the radial ion motion we will neglect both and consider collisionless deceleration in E_r .

The potential difference regarding an ion is given by

$$\int_0^r E_r dr.$$

Making a Galilean transformation, we can express the radial velocity in the sheet frame, in terms of experimental quantities, as

$$V_{ri} = U_s \left\{ 1 - \sqrt{\left(\frac{2e}{U_s m_i} \int_0^t E_r dt \right)} \right\}. \quad (25)$$

As the ions decelerate in E_r their number density will increase to satisfy mass conservation. Comparing this density to the microwave data then yields the ionization profile through the sheet, assuming that for steady flow the difference is due to a reduction in the local neutral population by ionization. The resulting ionization fraction can be expressed in the form

$$\alpha = \frac{n_e}{n_i + n_n} = \frac{n_e}{N_0} \frac{V_{ri}}{U_s}, \quad (26)$$

where N_0 is the filling density, n_e is the measured electron density, and V_{ri} is the local ion velocity calculated from (25). Figure 17 shows the ionization profile calculated in this fashion from experimental E_r , U_s , and n_e data in the centreplane. Similar profiles have been calculated from other axial positions, but we will restrict the remainder of this discussion to results for the centreplane.

The peak ionization is seen to occur at the peak current ($t = 0$), but the maximum value of ~ 3 is probably too high since triple ionization of all argon atoms in the sheet, though not absolutely excluded, is unlikely on energy grounds. This would require of the order of 100 eV/ion, allowing for excited states, whereas the kinetic energy of a neutral atom entering the sheet is only 130 eV. Spectroscopic studies confirm the existence of third ions, but not a large population. For these reasons, and also to be consistent with the single ionization assumption

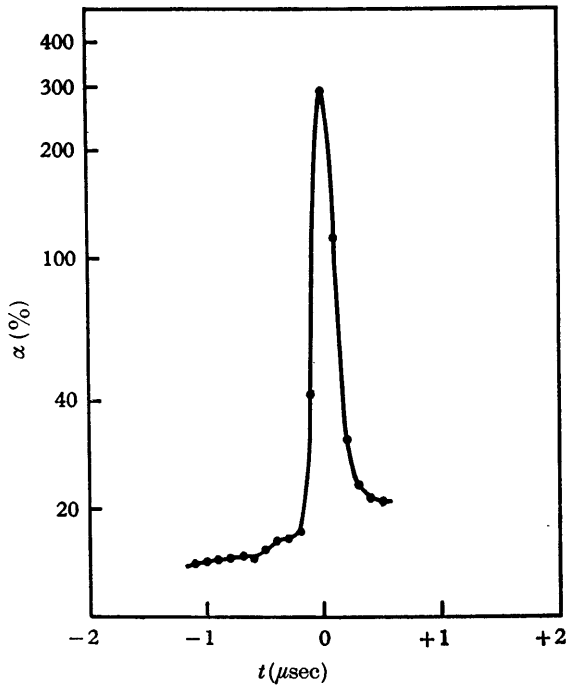


FIGURE 17. Ionization profile calculated from equation (26) (mid-radius centre plane).

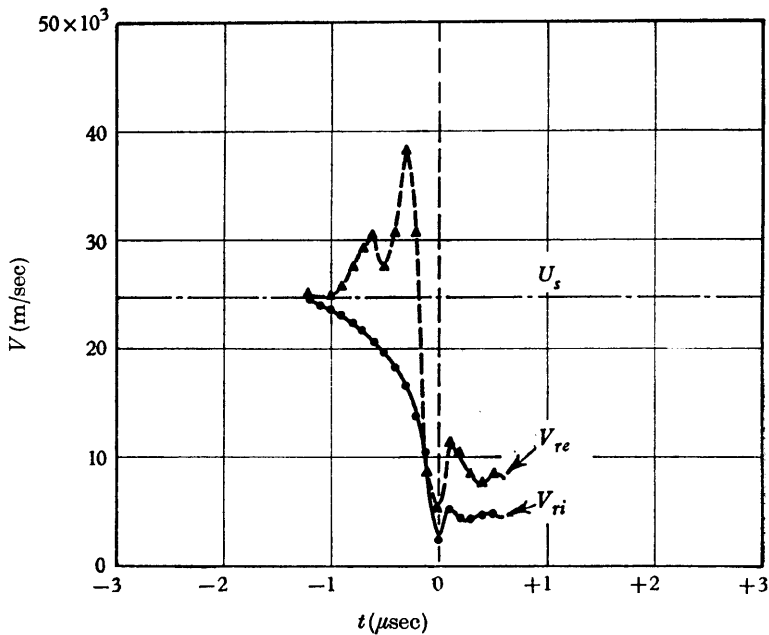


FIGURE 18. Radial ion and electron velocities (mid-radius centre plane).

inherent in (1), we will assume $Z = 1$ and restrict α to unity; this means that V_{ri} must be smaller in the centre of the current sheet than is predicted by the collisionless model, equation (25). The ion velocity profile 'corrected' for $\alpha = 1$ at $t = 0$ is shown in figure 18, and the stream deceleration is seen to be substantial, though not complete. In the laboratory frame the over-run ions are accelerated from rest to $\sim 0.8U_s$, or 20,000 m/sec.

Also plotted in figure 18 is the radial electron velocity,

$$V_{re} = \frac{j_z}{\sigma_0 B_\theta} - \frac{E_z}{B_\theta} \quad (27)$$

obtained from combining (23) and (24) with the defining relations

$$j_r = n_e e (V_{ri} - V_{re}), \quad (28)$$

$$j_z = n_e e (V_{zi} - V_{ze}). \quad (29)$$

These velocity profiles describe qualitatively similar behaviour for the electron and ion fluids through much of the sheet, both undergoing strong decelerations into the central region and slight acceleration out, even though V_{re} and V_{ri} are calculated completely independently, no quantity in (27) appearing in either (25) or (26). The difference between these curves is proportional to the radial current density, a rather irregular quantity in this model which is generally much smaller than j_z . If we had suppressed j_r by setting it equal to zero in (23), we would have found that V_{ri} as well as V_{re} was given by (27), since both species would then have the same radial velocity. But an initial acceleration of the ions in a retarding electric field, in the view of discussions above, is clearly unrealistic, so that j_r , though small, represents an important 'degree of freedom' in the problem.

Assuming V_{ri} (figure 18) to be correct, equations (9) and (23)–(29) can be manipulated to yield the axial electron and ion current densities in terms of known quantities,

$$j_{zi} = \frac{1}{B_\theta} \left(n_e e E_r + \frac{\partial P_e}{\partial r} \right) - \frac{n_e e}{\Omega_e} \left(\frac{E_z}{B_\theta} + V_{ri} \right) + \frac{1 + \Omega_e^2}{\Omega_e^2} j_z, \quad (30)$$

$$j_{ze} = \frac{1}{B_\theta} \left(n_e e E_r + \frac{\partial P_e}{\partial r} \right) - \frac{n_e e}{\Omega_e} \left(\frac{E_z}{B_\theta} + V_{ri} \right) + \frac{1}{\Omega_e^2} j_z, \quad (31)$$

in which form they resemble expansions in the reciprocal Hall parameter, and contain the familiar E_r/B_θ crossed field drift solution for the electrons as a special case ($P_e \rightarrow 0$, $\Omega_e \rightarrow \infty$).

Figure 19 shows the calculated axial current distribution for electrons and ions in the centre plane, with the j_z profile from the B probe data (equation (11)) superimposed. The large number of calculations involved introduces some unavoidable errors, but the indication seems clear that electrons are favoured to conduct the bulk of the axial current near the centre of the sheet, with ions dominating in the rear and participating to a lesser degree near the front. The electrons tend to flow in an inner layer which is narrower than the sheet itself, as defined by the sensible

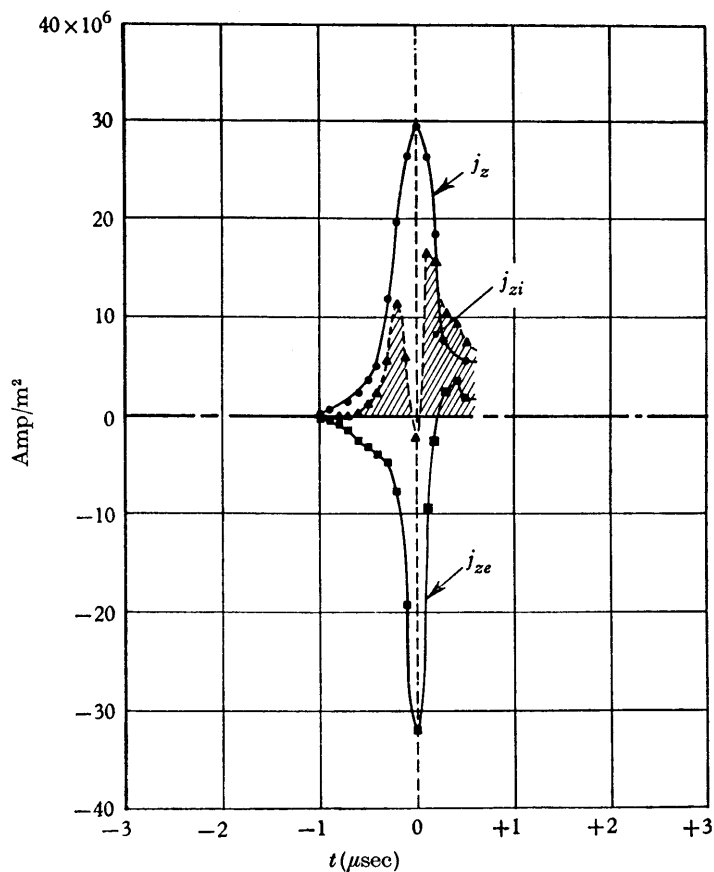


FIGURE 19. Calculated distribution of axial ion and electron current density (mid-radius centre plane).

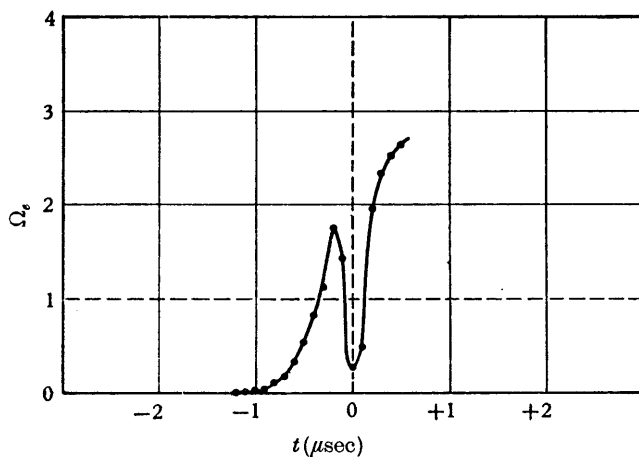


FIGURE 20. Electron Hall parameter (mid-radius centre plane).

current density, and of about the same width (~ 1 cm) as the electron density, temperature, and ionization profiles previously encountered. This similarity in profile widths has the important consequence that the electron Hall parameter varies in the same way as the electron and ion currents divide.

The Hall parameter is plotted in figure 20, and the rising B_θ field (figure 3) is seen to drive Ω_e from 0 to ~ 3 at the rear of the sheet. Embedded in, and giving rise to this magnetic field, is the axial current, which at its peak drives charges in such numbers that their frequent binary collisions weaken the hold of the growing magnetic field, and depress the Hall parameter well below unity. Therefore two regions appear in the sheet wherein the electrons experience multiple collisions during one gyro-period: the centre region where the density is high, and the leading edge where the magnetic field is small. In these regions the electrons should conduct essentially scalar current along the resultant \mathbf{E} field, of a magnitude determined by the local mobility. This explains, for example, why electrons in the front part of the sheet gain velocity initially in the prescribed (i.e. measured) E_r field that decelerates the ions (figure 18), although this will have the effect of weakening E_r .

On the other hand, the two regions where $\Omega_e > 1$ are seen to be just those regions where ion currents are important, and the close relationship between Ω_e and the ion current distribution suggests that when the electron Hall parameter is above unity the electrons are too greatly hindered by the magnetic field to conduct the required axial current. At the rear of the sheet, where Ω_e reaches its largest value, the small net current is carried almost entirely by ions. Thus it seems that Ω_e may be a simple and sensitive guide to the relative partitioning of current between electrons and ions in a current sheet.

The difficult problem of ion collisions is dealt with rather simply in the above model, in which no explicit reference is made to the ion Hall parameter. The relevant collision frequency for Ω_i is that of ions against neutrals, and ν_{in} is a complicated, anisotropic function of position due to the neutral-braking mechanism discussed above and the rapidly changing populations of ion and neutral atoms. A more detailed model of current sheet structure should treat these effects on a more elegant level and incorporate Ω_i explicitly (e.g. (1)). In addition, if ion slip effects are allowed, then the added complication of charge exchange collisions must also be taken into account.

6. Summary and conclusions

Electron and ion density distributions, and the problem of electron/ion current partitioning have been studied in a large radius Z -pinch discharge in argon. At a filling pressure of 0.1 torr, the imploding current sheet is ~ 2.5 cm wide, with a velocity of $\sim 2.5 \times 10^6$ cm/sec at the halfway point of its radial trajectory where the measurements were made.

The electron density and temperature are measured with a new multi-purpose type of microwave reflexion interferometer which returns information on the complex reflexion coefficient from the plasma. The probing horn is used to scan radially through the passing current sheet, and at the operating frequency of

70 GHz resolves densities up to 10^{17} cm^{-3} over dimensions of $\sim 4 \text{ mm}$. Measured electron density profiles through the sheet generally resemble the corresponding j_z profiles from B -probe data, but are steeper and narrower in all cases. The current sheet photoionizes the gas ahead of itself to $\sim 10\%$, producing a plasma whose density and temperature are known as it enters the current sheet, and whose collision frequency is dominated by electron-ion encounters for all times of interest. Typically n_e increases from $\sim 5 \times 10^{14} \text{ cm}^{-3}$ at the front of the sheet to $\sim 5 \times 10^{16} \text{ cm}^{-3}$ at peak current, over-riding the much smaller changes in T_e , at most a few eV, and thereby controlling the collision frequency, and through it the Hall parameter.

The electric and magnetic field distributions in the sheet are measured by standard techniques as functions of time, and from these the corresponding radial profiles are obtained. The measured electric field has both radial and axial components, from the combined effects of finite conductivity and a slight internal polarization, and in the sheet frame E_z is non-zero, though usually smaller than E_r . The magnetic field by contrast is purely azimuthal, and increases monotonically through the sheet.

These data are used to calculate electron and ion velocity components from a generalized Ohm's Law for the plasma. The analysis shows that within the approximations of MHD theory, the current sheet is built up of four inner layers alternately dominated by axial electron or ion current. This structure is observed to be closely correlated with variations of the Hall parameter, ω_b/ν_e , about the value of unity through the sheet, which suggests that Ω_e , whose behaviour is primarily governed by B_θ and n_e , might be useful as a guide to the relative importance of ion conduction in pinching current sheets.

The authors gratefully acknowledge the help of many members of the staff of the Guggenheim Laboratories for the Aerospace Propulsion Sciences, Princeton University, in carrying out this work. In particular we would like to thank D. M. Tregurtha for his valuable assistance in the laboratory, D. Neiler for the photographs, and T. Poli for the illustrations.

This reserach was supported by NASA Research Grant NsG-306-63.

Appendix. Effect of magnetic fields and density gradients on the plasma reflexion coefficient

Two potentially serious sources of error in assuming an isotropic, homogeneous plasma for calculating reflexion coefficients are the influence of the azimuthal magnetic field on the plasma refractive index, and the effects of electron density gradients on the phase of the reflexion coefficient.

First consider the effect of B_θ . Since B_θ is normal to the propagation direction, the only permitted modes of propagation are for the so-called ordinary and extraordinary waves. The former describes the situation where the \mathbf{E} vector of the probing wave is locally collinear with B_θ , in which case the magnetic field does not hinder electron oscillations and the solution is identical to the isotropic case, equations (18) and (19). The extraordinary mode describes oscillations

normal to B_θ , in which case the refractive index takes the form (Heald & Wharton 1965)

$$\mu_{ex}^* = 1 - \frac{(\omega_p/\omega)^2}{1 - i(\nu_c/\omega) - \frac{(\omega_b/\omega)^2}{1 - (\omega_p/\omega)^2 - i\nu_c/\omega}} \quad (A 1)$$

which differs from the isotropic index by a term proportional to the square of the normalized electron gyrofrequency. For the probing frequency of 70 GHz and the maximum value of B_θ , $\sim 0.5 \text{ W/m}^2$ at the rear of the sheet, we find $(\omega_b/\omega)^2 \leq 0.04$. This low value suggests that anisotropy effects will be unimportant at the probing frequency, and more exact calculations (Ellis 1967) of the reflexion coefficient show this to be correct for densities above n_c , as occur in the current sheet. Skin depths, calculated from the imaginary part of the index, $d = 1/k_0\mu_i$, also show negligible dependence on B_θ , so that the predicted penetration of the waves agrees with the isotropic result. Finally, identical experimental results were obtained for $|R|$ and S regardless of horn orientation, and so the isotropic theory was used for data reduction.

The validity of assuming plane boundaries for the reflecting plasma can be examined by using a more detailed model which incorporates the possibility of thermal boundary layers or similar transition zones embodying free electron density gradients near the plasma interface through which the probing wave-train must pass. The adiabatic or WKB approximation is useless here, since these methods suppress reflexion and interference effects which are the essence of the problem. The inhomogeneous zone must be examined explicitly to determine permitted modes of propagation through prescribed gradients normal to the horn window.

For gradients in the z -direction the refractive index can be written in the form

$$\mu^{*2}(z) = 1 - (1 - \mu_\infty^{*2})n_e(z)/n_{e\infty}. \quad (A 2)$$

Albini & Jahn (1961) have shown that the width of the zone is more important than its detailed profile shape, so that within reasonable limits $n_e(z)$ can be chosen as the best compromise between an adequate physical model and the necessary mathematical tractability. For this calculation an inverse exponential profile,

$$n_e(z) = n_{e\infty}[1 - \exp(-2mz/\lambda_0)] \quad (A 3)$$

was selected. This profile, whose derivatives are continuous and steepest at the boundary, reverts to either a linear ramp (Albini & Jahn 1961) or a plane slab by appropriate choices of the parameter m . The wave equation in the transition layer takes the form

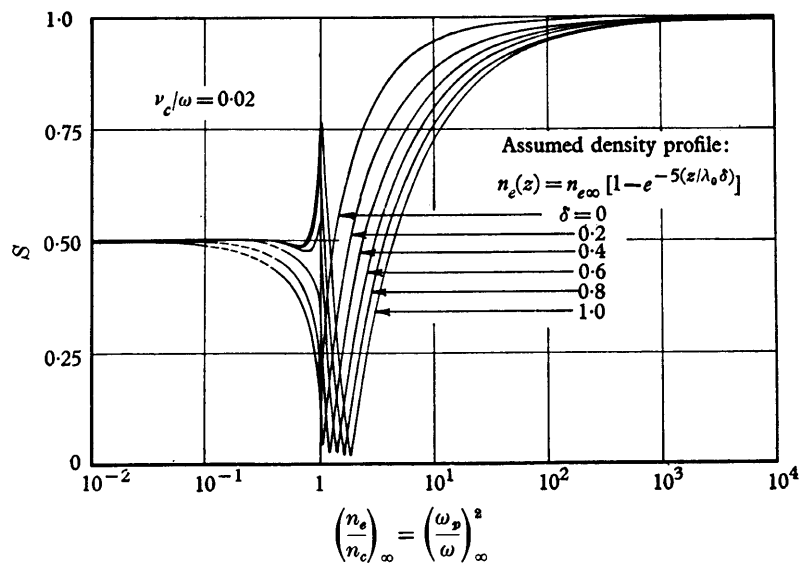
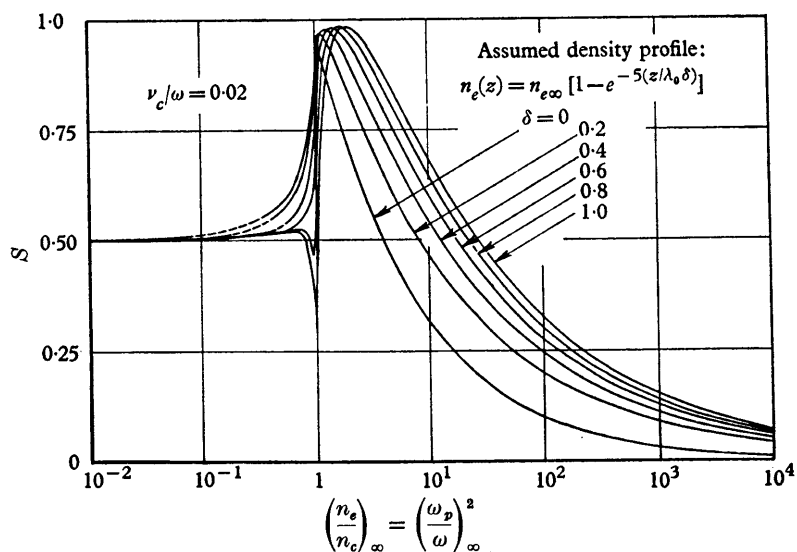
$$\frac{d^2 E}{dz^2} + k_0^2 \{1 - (1 - \mu_\infty^{*2})[1 - \exp(-2mz/\lambda_0)]\} E = 0 \quad (A 4)$$

which by change of variable

$$V = (\lambda_0 k_0/m)(1 - \mu_\infty^{*2})^{\frac{1}{2}} \exp(-mz/\lambda_0) \quad (A 5)$$

reduces to standard Bessel form (Watson 1952) with solution

$$E = AJ_p(V) + BJ_{-p}(V), \quad (A 6)$$

FIGURE 21. Theoretical interferometer response, *A* mode, diffuse boundary.FIGURE 22. Theoretical interferometer response, *B* mode, diffuse boundary.

where

$$p = i \frac{\lambda_0 k_0}{m} \mu_\infty^* \quad (\text{A } 7)$$

is the complex order of the Bessel functions, and A and B are arbitrary constants. Application of the boundary conditions that the fields be continuous at $z = 0$ and bounded at $z = \infty$ and the use of standard recursion relations (Watson 1952) leads to the reflexion coefficient in the form

$$R^* = \frac{(1 - \mu_\infty^*) J_p(\chi) + i(1 - \mu_\infty^{*2})^{\frac{1}{2}} J_{p+1}(\chi)}{(1 + \mu_\infty^*) J_p(\chi) - i(1 - \mu_\infty^{*2})^{\frac{1}{2}} J_{p+1}(\chi)}, \quad (\text{A } 8)$$

where χ is the dimensionless group

$$\chi = (\lambda_0 k_0 / m) (1 - \mu_\infty^{*2})^{\frac{1}{2}} \quad (\text{A } 9)$$

and μ_∞^* is the refractive index far from the boundary, given by equations (18) and (19). To specify the ramp width we can use m or the quantity δ , defined by noting that the electron density reaches 99 % of its uniform value when the total exponent of (A 3) is 5.0. Hence $\delta = 2.5/m = (z/\lambda_0)_{0.99n_{e\infty}}$ is a handy way of specifying the thickness of the transition zone in units of λ_0 , the free space wavelength. Figures 21 and 22 show the phase measurable S which would be obtained in the A and B modes, and the effect of wider ramps for above-critical densities is seen to be a general displacement of the curves to the right. An important feature of these curves is their asymmetry about $S = 0.5$, due to the non-linear definition of the phase measurable in equation (22). By assuming $\delta = 0, 0.2, 0.4$, etc., one can compute n_e distributions through the current sheet from data obtained in both A and B modes, and in general this will yield quite different curves. Since $n_e(r)$ must be independent of the measuring technique, the ramp width δ can be calculated as a function of position through the sheet by determining which A and B mode curves match n_e at any given time. The results of such calculations are that $\delta = 0$ matches the n_e profiles at all times within experimental error, $\delta = 0.2$ produces an order of magnitude discrepancy, and high values produce even larger errors. Although the selection of δ could be made more precise by iterating between calculated S curves parametrized alternately by δ and v_c/ω , the conclusion seems clear that the appropriate model for these experiments is the slab boundary, and so the simpler theory was used for data reduction.

REFERENCES

- ALBINI, F. A. & JAHN, R. G. 1961 *J. Appl. Phys.* **32**, 75.
 BLACK, N. A. 1965 Linear pinch driven by a high current pulse-forming network. *AIAA Bull.* **2**, 6, 309.
 BLACK, N. A. 1966 *Dynamics of a Pinch Discharge Driven by a High Current Pulse-forming Network*. Princeton Univ. Aeron. Rept 778, Princeton, N.J.
 BODIN, H. A. B., NEWTON, A. A. & PEACOCK, N. J. 1961 *Nuclear Fusion* **1**, 139.
 BODIN, H. A. B. & NEWTON, A. A. 1963 *Phys. Fluids* **6**, 1338.
 BURKHARDT, L. C. & LOVBERG, R. H. 1962 *Phys. Fluids* **5**, 341.
 BURTON, R. L. & JAHN, R. G. 1968 *Phys. Fluids* **11**, 1231.
 ELLIS, W. R. 1967 *An Investigation of Current Sheet Structure in a Cylindrical Z-pinch*, Princeton Univ. Aeron. Rept 805, Princeton, N.J. Ph.D. Thesis, Princeton University.
 FUNAHASHI, A. & TAKEDA, S. 1968 *J. Appl. Phys.* **39**, 217.

- HEALD, M. A. & WHARTON, C. B. *Plasma Diagnostics with Microwaves*. New York: Wiley and Sons.
- HERMANSDORFER, H. 1965 *Measurement of High Electron Densities in a Linear Z-pinch using a New Microwave Reflection Probe*. Report IPP 1/37, Institut für Plasmaphysik, Garching.
- HUDDLESTONE, R. H. & LEONARD, S. L., eds. 1965 *Plasma Diagnostic Techniques*. New York: Academic Press.
- JAHN, R. G. *et al.* 1965 *Rev. Sci. Instrum.* **36**, 101.
- JAHN, R. G. 1962 *Phys. Fluids* **5**, 678.
- JAHN, R. G. 1960 *Interaction of Electromagnetic Waves with Slightly Ionized Gases*. Guggenheim Jet Propulsion Center, California Institute of Technology, Report TN-2.
- JAHN, R. G. *et al.* 1968 *Pulsed Electromagnetic Gas Acceleration*. 12th Semi-annual progress report for the period 1 January 1968 to 30 June 1968, Princeton University Aerospace and Mechanical Science Report no. 634k, July 1968. *Ibid.* Reports no. 634h, 634j.
- JOHANSSON, R. B. 1965 *Phys. Fluids* **8**, 866.
- LOVBERG, R. 1963 *Proceedings of VI International Conference on Ionization Phenomena in Gases* (Paris, 1963), vol. iv, pp. 235.
- LOVBERG, R. 1966 *AIAA J.* **34**, no. 7, 1215.
- LOVBERG, R. 1964 *Phys. Fluids* **7**, S 57.
- SLATER, J. C. 1959 *Microwave Transmission*. New York: Dover Publications.
- SPITZER, L. 1962 *Physics of Full-Ionized Gases*, 2nd ed. New York: Interscience.
- SUTTON, G. W. & SHERMAN, A. 1965 *Engineering Magnetohydrodynamics*. New York: McGraw-Hill.
- TAKEDA, S. & TSUKISHIMA, T. 1965 *Microwave Reflection Techniques for Dense Plasma Diagnostics*. U.S. National Bureau of Standards Report NBS-256.
- WATSON, G. N. 1952 *A Treatise on the Theory of Bessel Functions*. New York: Cambridge University Press.
- YORK, T. M. 1968 *Pressure Distributions in the Current Sheet Structure of a Dynamic Pinch Discharge*, Ph.D. Thesis, Princeton Univ.